Light source distribution and scattering phase function influence light transport in diffuse multi-layered media

Fabrice Vaudelle, Jean-Pierre L'huillier, Mohamed Lamine Askoura

Light source distribution and scattering phase function influence light transport in diffuse multi-layered media

Fabrice Vaudelle[a,*], Jean-Pierre L'Huillier[a], Mohamed Lamine Askoura[a,b]

[a] *Laboratoire LAMPA, Univ Bretagne Loire, Arts et Metiers ParisTech, 2 Boulevard du Ronceray, 49035 Angers cedex 01, France*
[b] *Unité de Recherche GRAPPE, Univ Bretagne Loire, Ecole Supérieure d'Agricultures (ESA)-INRA, 55 rue Rabelais, BP 30748, 49007 Angers Cedex, France*

Keywords:
Light propagation in turbid tissues
Photon migration
Human skin
Skin and flesh of apple tissues
Scattering measurements

A B S T R A C T

Red and near-Infrared light is often used as a useful diagnostic and imaging probe for highly scattering media such as biological tissues, fruits and vegetables. Part of diffusively reflected light gives interesting information related to the tissue subsurface, whereas light recorded at further distances may probe deeper into the interrogated turbid tissues. However, modelling diffusive events occurring at short source-detector distances requires to consider both the distribution of the light sources and the scattering phase functions. In this report, a modified Monte Carlo model is used to compute light transport in curved and multi-layered tissue samples which are covered with a thin and highly diffusing tissue layer. Different light source distributions (ballistic, diffuse or Lambertian) are tested with specific scattering phase functions (modified or not modified Henyey-Greenstein, Gegenbauer and Mie) to compute the amount of backscattered and transmitted light in apple and human skin structures. Comparisons between simulation results and experiments carried out with a multi-spectral imaging setup confirm the soundness of the theoretical strategy and may explain the role of the skin on light transport in whole and half-cut apples. Other computational results show that a Lambertian source distribution combined with a Henyey-Greenstein phase function provides a higher photon density in the stratum corneum than in the upper dermis layer. Furthermore, it is also shown that the scattering phase function may affect the shape and the magnitude of the Bidirectional Reflectance Distribution (BRDF) exhibited at the skin surface.

1. Introduction

Investigations on light-tissue interaction processes have been performed owing to multiple applications related to therapy and diagnosis in the medical field [1–4]. The rendering of object with computer graphics has been also improved with a better knowledge on the mechanisms of light propagation in turbid media [5]. Furthermore, the interest has been focused on the quality prospect of fruits and vegetables using diffusion models and non-invasive optical spectroscopy systems [6]. The use of red and near-infrared (NIR) light especially allows to probe deeply into interrogated turbid tissues [7], showing the possibility to extract spectral information on tissue constituents. In this wavelength range, several key optical parameters characterize the light propagation in turbid media [1]: the average refractive index (n_r), the absorption coefficient (μ_a), the scattering coefficient (μ_s), and the scattering phase function ($p(\theta)$). The absorption coefficient μ_a and scattering coefficient μ_s are respectively the number of absorption and scattering events per unit length, while the phase function $p(\theta)$ represents the angular distribution of a scattering event. When the diffusion is predominant [8], the so-called reduced scattering coefficient defined as $\mu'_s=\mu_s(1-g)$ is useful, where g (anisotropy factor) is the average cosine of the angular deviation. This leads to the fact that the transport length $1/\mu'_s$ describes the distance which light travels before the propagation direction be completely randomized due to scattering events. However, a rigorous treatment of the light propagation in turbid tissues requires to use the radiative transfer equation (RTE) still considering μ_a, μ_s and $p(\theta)$ [9]. Note that an exact solution of the RTE is difficult to find [10], notably due to the integro-differential form of this equation and regarding all the constraints related to the tissues (heterogeneities, structure, complex boundaries, and source-detector arrangements).

A usual way to solve the RTE is to use Monte Carlo (MC) method [11], which has the advantage to follow the photon paths according to probability functions. These probabilities estimate length of free paths, direction changes, absorption and Fresnel reflection for the different boundaries [11,12], and depend on the optical coefficients μ_s, μ_a, g, and n/n_{ext} (relative index of refraction). Monte Carlo methods have been widely used for several transport problems [13,14] and for numerical

* Corresponding author.
E-mail address: f.vaudelle@libertysurf.fr (F. Vaudelle).

http://dx.doi.org/10.1016/j.optcom.2017.02.001

Nomenclature

$\mu_s^{(i)}$	scattering coefficient of the layer (i)
$\mu'_s{}^{(i)}$	reduced scattering coefficient of the layer (i)
$\mu_t^{(i)}$	transport coefficient of the layer (i)
$\mu'_t{}^{(i)}$	reduced transport coefficient of the layer (i)
$\mu_a^{(i)}$	absorption coefficient of the layer (i)
g	anisotropy coefficient
γ	factor characterizing a phase function
p_{HG}	Henyey-Greenstein phase function
p_{GK}	Gegenbauer phase function
α	shape parameter of p_{GK}
g_{GK}	coefficient related to p_{GK}
p_{Mie}	phase function based on the Mie Theory
p_{MHG}	modified Henyey-Greenstein phase function
p_{MGK}	modified Gegenbauer phase function
α_{Iso}	proportion of symmetric component in the modified phase functions p_{MHG} and p_{MGK}
$p_{\delta E,Iso}$	delta-Eddington phase function
$p_O(\theta_O)$	exponentiated cosine distribution function
$p_b(z)$	distribution of ballistic light source along depth z
$p_{IsoForw}(z)$	distribution of diffuse light source along depth z
ω_0	source radius
r_s	spherical radius
θ	angular deviation
ρ	radial distance
z	axial distance (depth)
θ_O	angle defined only at the surface
(x_c, y_c, z_c)	coordinates related to the half-sphere geometry

simulations of photon propagation in multilayered biological tissues [15–19] or within tissue-like diffusing phantoms [20,21]. The knowledge of laser light transport through the human skin allows to improve therapy applications [17], cosmetic analysis [22], or to reproduce the human face with more accuracy [5]. In this last case, the specular and diffuse light coming from the location of the light source which illuminates the skin surface are studied with respect to different observation angles. The effects of the light source shape [23–25], surface roughness [26], optical-clearing [27] and hair density [28] on the photon dose absorbed in the human skin have been well investigated. However, to our knowledge, the influence of the angular distribution of the light source (ballistic, diffuse or Lambertian) on

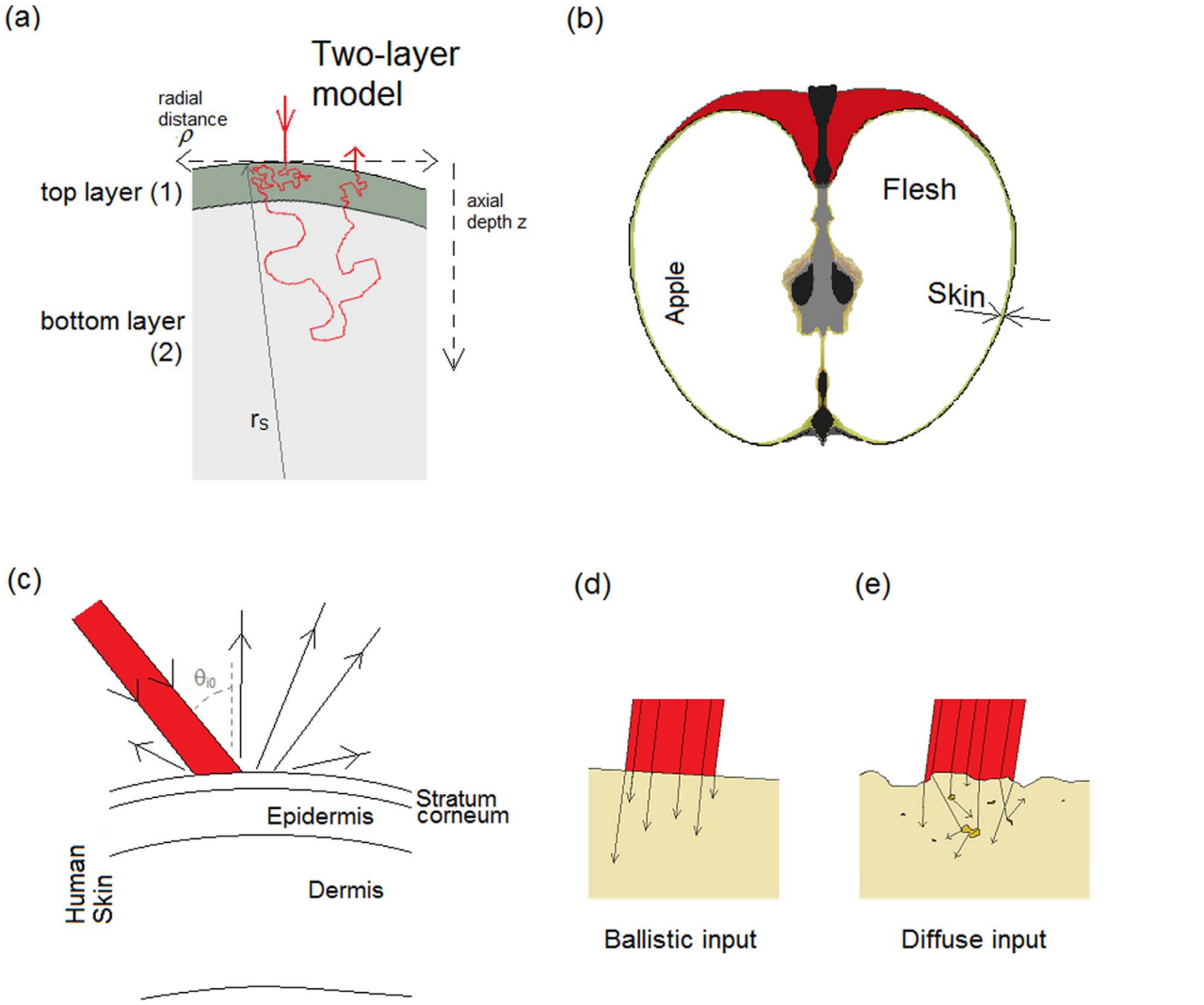

Fig. 1. Schematic pictures of multilayered tissue structures (a) Curved two-layer turbid medium with a top layer (skin), and illuminated by a laser source under normal incidence. (b) Example of top and bottom layers in biological tissues: apple with skin and flesh. (c) Simplified scheme of the human skin illuminated under oblique incident light source. (d) Ballistic and (e) diffusive light sources.

the light transport in the human skin structure has not yet been reported.

Monte Carlo simulations have been also designed to study the photon propagation in multi-layered fruits and vegetables [12,29–31]. The reflectance provided by a multispectral lighting of fruits can be related to quality attributes, such as bruise defects [32], firmness [33], ripeness [34], anti-oxidants concentration [35]. Often these studies need the non-invasive retrieval of the tissue optical parameters. To assess the optical coefficients of each tissue type (skin and flesh), the integrating sphere method [29,36] is well adapted. A non-invasive technique based on the light reflectance such as the meta-modelling [37] (which uses different optical properties of homogeneous intralipid solutions as reference data) does not take into account that the fruits have a multilayered tissue structure. Moreover, the inverse method applied to a two-layer diffusion model [38] is not available at proximity of the source, because the diffusion approximation fails for small source-detector distances. To better understand how reflectance measurement close to the light source are affected by the apple structure, a light propagation model requires to take into account the light source distributions but also adequate scattering phase functions [39–43].

In this paper, a modified Monte Carlo model is used in order to compute the light transport in multi-layered tissue samples. Different light sources including ballistic, diffuse, and Lambertian distributions are used with specific scattering phase functions to study the amount of backscattered and transmitted light in curved and multilayer tissue structures (apples and human skin). Comparisons between simulation results and experiments carried out with a multispectral imaging setup enable to choose light sources and phase functions that are best suited to describe the light transport in apple tissues (skin and/or flesh). The influences of the light source distributions and scattering phase functions on light transport in epidermis, stratum corneum, and dermis of a human skin model are also studied, with a special emphasis on the Bi-Directional Reflectance Distribution Function (BRDF).

2. Tissue models

The three investigated tissue models referring to the Monte Carlo are displayed in Fig. 1(a-b-c). Fig. 1(a) displays basic two-layer and curved tissue model (r_s=35 mm). This geometry introduces the difficulty to generate diffuse reflectance profiles (photons re-emitted at close and far radial distances ρ from the incident point) when the top layer is very thin and more diffusing compared to the bottom tissue. Monte Carlo simulations were performed with this model using different input data, for conditions that especially span the non-diffuse and intermediate regimes (see Section 4.1).

Fig. 1(b) shows the cross-sectional view of an apple, which constitutes the second investigation tissue structure. The whole fruit was modeled as a homogeneous sphere (radius r_s=35 mm) including the flesh and a surrounding thin top layer that mimics the skin (or epidermis). The half-cut apple, considered in the experiments and simulations described in Section 4.2.1, was modeled as the half of the previous sphere. Both models were also considered as “peeled” or “unpeeled”, in order to tentatively separate the combined optical effects due to the skin and the flesh on the lumped diffuse reflectance profile. The “peeled” tissue was simply simulated by assigning the same optical properties to the flesh and skin layers. Typically, the peel is made of flat cells whose sizes evolve rapidly from the surface to deep depths. The subsurface structure is mainly composed of cuticle, epidermis and several layers of hypodermis. Skin thickness values, reported by the literature, range from 50 to 100 μm [31,44,45], when the hypodermis is ignored. An average thickness of about 80 μm was chosen as a reference for the skin layer, in a great part of this study.

Different values of reduced scattering coefficient μ'_s and absorption coefficient μ_a related to the flesh and the skin of three apple cultivars "Royal Gala, Golden Delicious and Granny Smith" are listed in Table 1. The data concerning the flesh have been reported by authors who worked with the steady-state hyper spectral method or with the time-resolved reflectance method, for wavelengths ranging from 633 nm to 852 nm (~near infrared domain). The optical properties of skin (see Table 1) were adapted from one of the few investigations [36] that show results related to the separation of skin and flesh samples.

According to the data about the components of the human skin [49], a simple two-layer model may not be accurate enough to describe all the influence of the skin on the propagation of the light. The human skin is a multilayer tissue structure [49], whose components are mainly cell membranes, fibers and organelles. These components give strong scattering and absorbing properties for wavelengths ranging in the visible (Vis) domain. At the micro scale, the dry dead cells constitute the stratum corneum layer (~20 μm), which is above the first living tissues, the epidermis layer (~100 μm) followed by the dermis layer (~1–4 mm, with blood components). Some values of their optical properties are shown in Table 2. At the mesoscale, the roughness of the skin surface can provide a diffuse specular reflection, which is only negligible in the normal incidence case (~4–7% of the source intensity in the Vis domain). The model shown in Fig. 1(c) refers to these three tissue layers, but is drawn according to the curvature radius of 70 mm.

The biological tissues have an anisotropy factor g often close to the values g=0.8–0.9, but fruits and vegetables may have lower values [29,36] (between 0.5 and 0.8 for apple). The anisotropy factor of the three above described tissue models was chosen in this range of values. Finally, the refractive indexes n =1.4 and n_{ext} =1 were used for all turbid media and the outside, respectively, in agreement with those concerning the human skin (~1.4 [49]), and the apple tissues (1.37 [36]).

3. Monte Carlo model

3.1. Flowchart

The main code was adapted from the methods previously described by Wang et al. [11], and was implemented on MATLAB software. However, the code was modified to account for the spherical shape and

Table 1
Optical properties of studied apple cultivars (mm^{-1}).

Apples	Wavelengths	Flesh μ_a (2) (mm^{-1})	Flesh μ'_s (2) (mm^{-1})	Skin μ_a (1) (mm^{-1})	Skin μ'_s (1) (mm^{-1})	g (flesh)
Gala	750–850 nm	~ 0.1 ± 0.1 [36]	~ 1.2 [36]	~ 0.15 ± 0.1 [36]	3.75 [36]	~0.65 [36]
		~ 0.0125 [47]	1.15 ± 0.3 [47]			
	633 nm	~ 0.1 ± 0.1 [36]	~ 1.2 [36]	~ 0.5 ± 0.1 [36]	~ 4 [36]	~0.75 [36]
		~ 0.0125 [47]	1.2 ± 0.3 [47]			
Granny	750–850 nm	~ 0.04 ± 0.03 [36]	~ 1.2 [36]	~ 0.075 ± 0.03 [36]	4.25 [36]	~0.6 [36]
		~ 0.1 ± 0,1 [36]	~ 1.2 [36]	~ 0.5 ± 0.1 [36]	~ 4 [36]	~0.7 [36]
	633 nm	0.005 ± 0.0025 [46]	1.1 ± 0.1 [46]			
Golden	750–850 nm	~ 0.01 [48]	0.8 ± 0.1 [48]			
		~ 0.04 [48]	0.85 ± 0.15 [48]			
	633 nm	0.004 ± 0.0025 [46]	1.4 ± 0.15 [46]			

Table 2
Optical properties of the human skin model (mm^{-1}).

Skin layers	Wavelengths	μ_a (mm^{-1})	μ_s (mm^{-1})	g	Thickness
Stratum corneum	400 nm [49]	23	200	0.9	~20 μm
	633 nm [17]	~0.7	100	0.86	
	650 nm [50]	0.8	50	0.936	
Epidermis	633 nm [49]	3.5	45	0.8	~100 μm
	633 nm [17]	~0.8	45	0.8	
	650 nm [50]	0.1–1.5	5.5	0.79	
Dermis	633 nm [49]	0.27	19	0.8	~1–3 mm
	633 nm [17]	~0.15	25–30	0.8–0.9	
	650 nm [50]	0.6	5.6	0.715	

boundaries of the different investigated tissue models (Fig. 1(a-b-c)). Moreover, the code was also modified to provide a choice in four specific scattering phase functions (see Section 3.2.3) and different axial, radial and angular light source distributions (see Sections 3.2.1 and 3.2.2). This allows the user to select a specific phase function and a light source distribution at the surface (step 0) with a given axial source distribution (step 1). The number of launched photons used in the different simulations reported below, depends on the configuration and can be varied from 0.5 to 2.10^6. The boundaries, over which the photons are recorded, were only spherical (radius 35 or 70 mm) or spherical-planar (for instance adapted to sliced fruit). Each model (Fig. 1(a)) was also considered with and without a thin top layer.

As long as the incident light direction is not deflected inside the tissue, the propagation is assumed as ballistic (Fig. 1(d)). Owing to the surface roughness and the in homogeneities inside the subsurface, all the incident photons have not the same direction. Therefore, the surface or the subsurface diffuse the incident light, in such a way that the source appears as an isotropic source (Fig. 1(e)). In the stochastic Monte Carlo scheme, the photons which have experienced a first step of propagation can be seen as ballistic or diffuse. The source was introduced with a statistical distribution along the normal axis Oz (vertical incident direction) with an exponential law of probability (μ'_t *or* μ_t)exp[-(μ'_t *or* μ_t)z], where $\mu_t=\mu_s+\mu_a$ and $\mu'_t=\mu_s'+\mu_a$ are the transport and the reduced transport coefficients, respectively. The value of $\mu_t^{(i)}$, or $\mu_t^{(i)\prime}$, depends on the photon's location in the traveled tissue layer (i=1, 2 or 3), i.e. computed from the sets ($\mu_s^{(i)}$, $\mu_a^{(i)}$).

The fundamental steps of the Monte Carlo model are summarized in the flowchart depicted in Fig. 2. That implies the use of the test named as “Russian roulette” when the threshold of the life weight is reached. This threshold has been put at 80% with respect to the initial life weight, which enables to use the test even at small source-detector distances. Note that with an albedo always larger than 0.97 in this work, the photon weight variance will only play its effect when a great number of scattering events occurs. In contrast, the influence of the scattering phase function and the source distribution should be maximal for the cases where a little number of scattering events prevails (ballistic, intermediate or subdiffusive regimes [21,43]), particularly at very small source-detector distances.

3.2. Light source models and Scattering phase functions

3.2.1. Source distributions inside the tissues

The first solution to the problem of the forward peak in the scattering studies was the introduction of the delta function [51,52]. For a system with an anisotropy g, the delta-Eddington function [52] combines an isotropic diffusion with a forward collimation as described by the following equation:

$$p_{\delta E,Iso}(\theta) = \frac{1}{4\pi}[1-g+2g\delta(1-\cos\theta)] \quad (1)$$

Indeed, the input event in the turbid medium can take into account this function. It may be interpreted as the fact that a diffuse source is related to an anisotropic propagation in a turbid medium if the similarity relation $\mu'_s=\mu_s(1-g)$ occurs. So, the diffuse source (Fig. 1e) may decrease following an exponential law as is the case of the ballistic source, when μ_s is changed to μ'_s. The ballistic source and diffuse source (called now *IsoForw*) are defined at the initial steps of the Monte Carlo code (Fig. 2): {step 1: ballistic probability $p_b(z)=\mu_t \exp(-\mu_t z)$ with phase function $p(\theta)$} or {step 1: $p_{IsoForw}(z)=\mu'_t \exp(-\mu'_t z)$ with random polar angle}, respectively. For this second probability scheme, the incident photons coming from the source propagate on deeper distances and then isotropically diffuse. This source distribution $p_{IsoForw}$, which is only used for the first scattering event of the incident photons, will give a different reflectance at proximity of the source than the one related to a ballistic distribution (p_b). In order to adapt these probabilities to the two-layered tissues, the axial distributions of the incident photons will be defined as the probability densities

$$p_b(z) = [\mu_t^{(1)} e^{-\mu_t^{(1)} z} + (e^{-\mu_t^{(1)} L} - 1) H(z-L)] H(L-z) + \mu_t^{(2)} e^{-\mu_t^{(2)}(z-L)} H(z-L) \quad (2)$$

$$p_{IsoForw}(z) = [\mu_t'^{(1)} e^{-\mu_t'^{(1)} z} + (e^{-\mu_t'^{(1)} L} - 1) H(z-L)] H(L-z) + \mu_t'^{(2)} e^{-\mu_t'^{(2)}(z-L)} H(z-L) \quad (3)$$

where H is the Heaviside distribution, and L the thickness of the skin layer.

3.2.2. Source distributions at the tissue surface

Concerning the step 0 (Fig. 2), the source may be characterized by a Gaussian [53] or a uniform radial shape. Both profiles are simulated

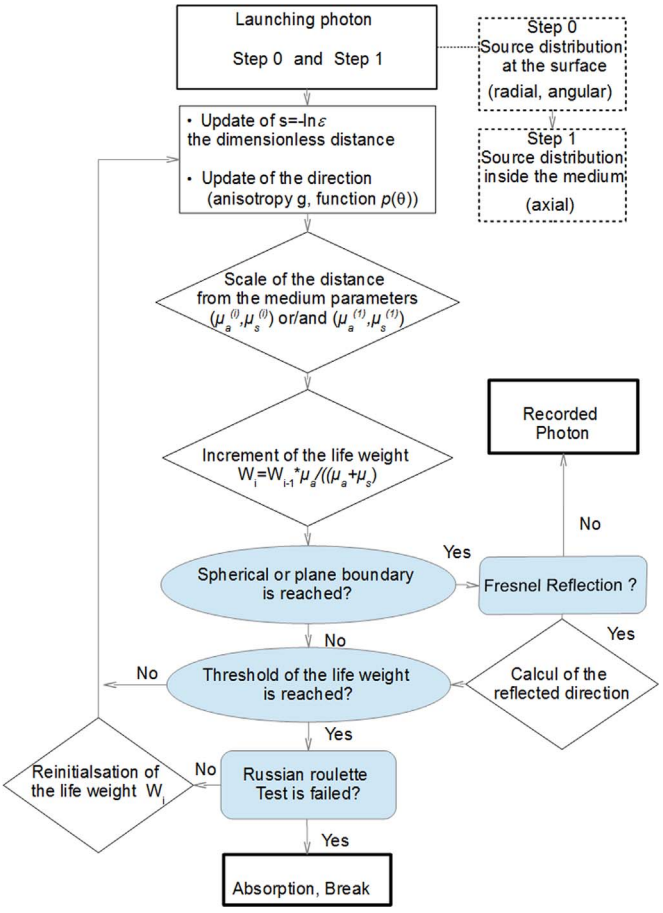

Fig. 2. Flowchart of the Monte-Carlo model including two components of the light source distribution: surface (step 0) and volume (step 1), (ε is a random number).

thanks to a random number $0 < v < 1$, from which the radial coordinate ρ is defined as follows:

$$\rho = \omega_0[A\left(\frac{-\ln v}{2}\right)^{1/2} + (1-A)v] \tag{4}$$

where $\omega_O/2$ is the standard deviation of the Gaussian (A=1) or the half-radius of the uniform (A=0) radial distributions. In both cases the beam size of the incident radiation used here was set at ω_O=0.5 mm. Note that the modelling of a realistic Gaussian laser source is an important task for imaging problems using a Monte Carlo code [20].

Another effect can be easily simulated at this step 0: the random angular variation of an angle θ_O around the normal direction of the optical axis that occurs at the surface due to the irregular surface or due to a diffuse illumination. The exponentiated cosine distribution function defined by

$$p_0(\theta_0) = H\left(\frac{\pi}{2} - \theta_0\right)(n+1)\frac{\cos(\theta_0)^n}{2\pi} \tag{5}$$

allows random angular variations of θ_O [54]. Its influence increases as the parameter n (entire) decreases.

3.2.3. Scattering phase functions

Regarding a homogeneous medium with a smooth surface, a ballistic light source gives a model more proper than an isotropic point source in order to study the reflectance at proximity of the source. Along the axis Oz, the probability density $\mu_t \exp(-\mu_t z)$ describes well this source. But whatever initial positions of incident photons, the isotropic diffusion is established far from the source in turbid tissue. The transfer from a ballistic input to an isotropic light diffusion depends on the choice of the scattering phase function $p(\theta)$, i.e. the probability density to change the direction. The phase function density can be represented by the following series:

$$p(\theta) = \frac{1}{4\pi}\sum_n (2n+1) g_n P_n(\cos\theta) \tag{6}$$

with

$$g_n = 2\pi \int_0^\pi p(\theta) P_n(\cos\theta)\sin\theta \, d\theta \tag{7}$$

where P_n is the polynomial Legendre function of order n. The first order g_1 is the mean cosine of the scattering angle θ, i.e. the anisotropy coefficient g. The following functions, p_{HG}, p_{GK}, p_{Mie}, p_{MHG} and p_{MGK}, are considered in this study according to their specificities.

The phase functions found with symmetrical scattering (as Rayleigh scattering) or with forward enhancement (as Mie scattering) have often small or extended orders g_n, respectively. The Mie phase function [55], $p_{Mie}(\theta)$, is obtained from the Mie diffusion theory, and it can be numerically estimated from one sphere of radius a or from a radii distribution. The Henyey-Greenstein function $p_{HG}(\theta)$ [56], (where $g_n = g^n$), is often used for highly scattering media:

$$p_{HG}(\theta) = \frac{1}{4\pi}\frac{1-g^2}{(1+g^2-2g\cos\theta)^{3/2}} \tag{8}$$

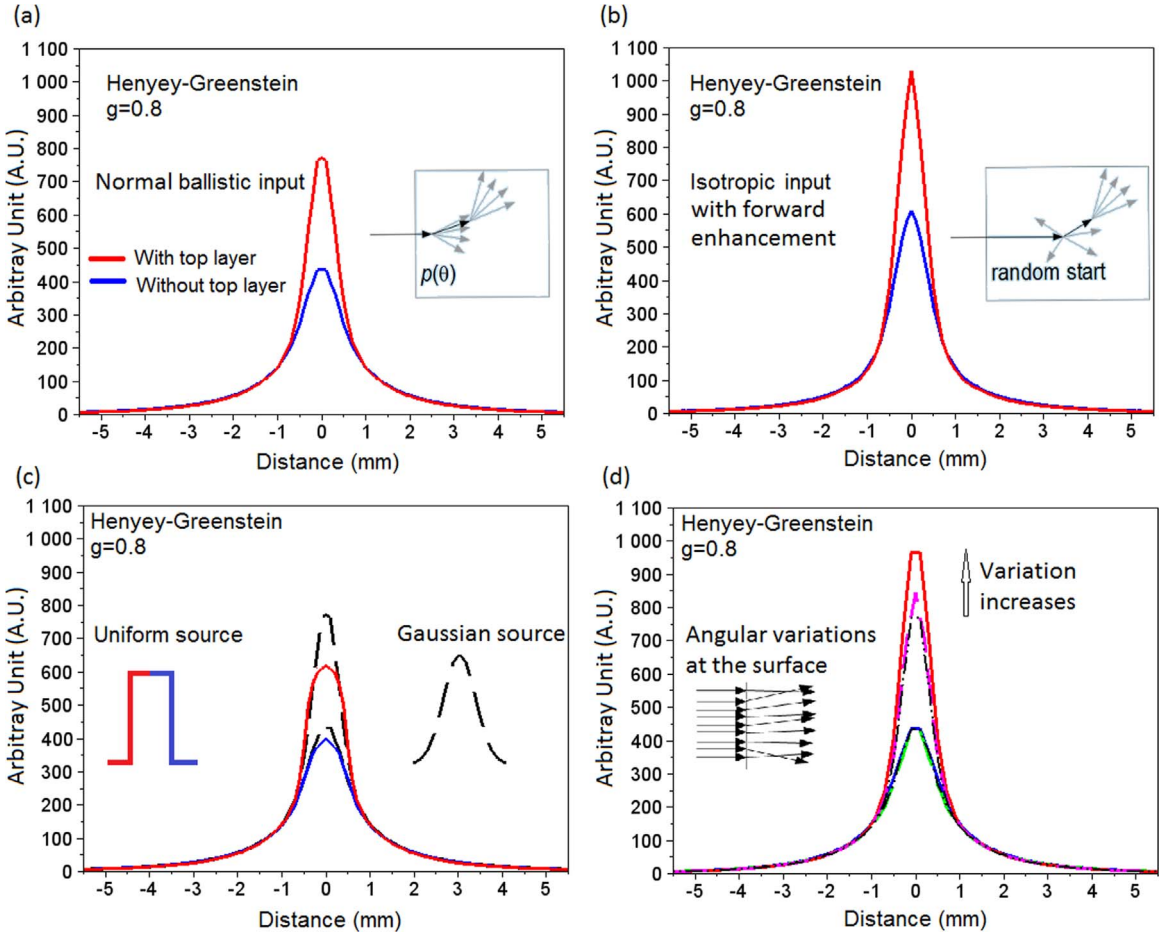

Fig. 3. Reflectance profiles generated with a skin thickness of 80 μm (red, purple dashed lines) and without skin (blue, dashed green lines), with $\mu_a^{(2)}$=0.0095 mm^{-1}, $\mu'_s{}^{(2)}$=1.12 mm^{-1}, $\mu_a^{(1)}$=0.05 mm^{-1}, $\mu'_s{}^{(1)}$=4 mm^{-1}, and for different light source distributions. (a) Gaussian light source with ballistic depth distribution (Eq. (2)). (b) Gaussian light source with diffuse depth distribution (Eq. (3)). (c): Uniform light source with ballistic depth distribution (Eq. (2)) (black dashed lines linked to (a)). (d) Gaussian light source with angular surface distributions (Eq. (5)) for n=2, n=20 (dashed lines) and n=infinite (black dash-dotted lines), and with ballistic depth distribution (Eq. (2)). (For interpretation of the references to color in this figure legend, the reader is referred to the web version of this article).

The Gegenbauer kernel function [57] $p_{GK}(\theta)$, run by α and g_{GK} coefficients, is defined by

$$p_{GK}(\theta)=\frac{\alpha g_{GK}}{\pi[(1+g_{GK})^{2\alpha}-(1-g_{GK})^{2\alpha}]}\frac{(1-g_{GK}^2)^{2\alpha}}{(1+g_{GK}^2-2g_{GK}\cos\theta)^{\alpha+1}} \quad (9)$$

The modified Henyey-Greenstein (or Gegenbauer) phase functions are built on the idea that the Henyey-Greenstein (or Gegenbauer) function, $p_{HG}(\theta)$ (or $p_{GK}(\theta)$), which represents essentially the forward part, should be added to another phase function which characterizes the backscattering part. This last can be a constant value [58], a function linked to the Rayleigh diffusion [40], or another Henyey-Greenstein function with a negative coefficient of anisotropy [41]. The Modified Henyey-Greenstein $p_{MHG}(\theta)$ [40,42], used here and depending on α_{Iso} coefficient, is:

$$p_{MHG}(\theta)=(1-\alpha_{Iso})\cdot p_{HG}(\theta)+\alpha_{Iso}\frac{3}{4\pi}\cos^2\theta \quad (10)$$

The Modified Gegenbauer $p_{MGK}(\theta)$ is defined as $p_{MHG}(\theta)$ when the Gegenbauer Kernel function $p_{GK}(\theta)$ replaces $p_{HG}(\theta)$.

4. Simulation results and discussion

4.1. Two-layer curved tissue

In this subsection the two-layer diffusing medium depicted in Fig. 1(a) is considered. The thicknesses of the top and bottom layers were kept to 80 μm and 35 mm, respectively (in accordance to the curvature radius r_s=35 mm). Unless otherwise specified, Monte-Carlo simulations were performed using the following optical parameter sets:- top layer $\mu_a^{(1)}$=0.05 mm^{-1}, $\mu'^{(1)}_s$=4 mm^{-1}- bottom layer $\mu_a^{(2)}$=0.0095 mm^{-1}, $\mu'^{(2)}_s$=1.12 mm^{-1} and g=0.8. In all simulations the reflectance profile was computed as the number of photons exiting a surface element of 0.1×0.1 mm^2. This simple tissue model offers the opportunity for understanding how the computed reflectance profile may be affected by the light input parameters, by the scattering phase functions, and also by the presence of the thin top layer. To this end, for all the results shown in Fig. 3(a-b-c-d) and Fig. 4(b-c-d) the reflectance profiles were computed by considering the tissue with and without top layer. In this last case, the optical properties of the top layer were simply the same as those assigned to the bottom layer.

4.1.1. Effects of light source distributions

Monte Carlo simulations were run assuming the Henyey-Greenstein phase function, $p_{HG}(\theta)$ (see Eq. (8)). Fig. 3(a-b) shows the influence of the axial light distribution (Eqs. 2–3) on the radial reflectance profile, for a Gaussian source shape acting at the tissue surface. Fig. 3(c-d) shows the effect of different light source distributions at the tissue surface (Eqs. 4–5) on the reflectance profile, using axial ballistic light propagation.

It can be observed that the peak intensity computed for the two-layer tissue is almost twice the one related to the simple bottom layer. This ratio remains unchanged when the top layer absorption is fixed at 0.05 mm^{-1} or even at 0.5 mm^{-1}. This may be explained by the too low propagation length experienced by the photons propagating close to the source axis. In order to refine these observations, other optical parameter sets of the bottom layer were tested: $\mu_{amin}^{(2)}$=0.0025 mm^{-1} - $\mu'^{(2)}_s$=1.45 mm^{-1}, [$\mu_{amin}^{(2)}$, 3$\mu_{amin}^{(2)}$, 9$\mu_{amin}^{(2)}$] - $\mu'^{(2)}_s$=1.25 mm^{-1}, and 3$\mu_{amin}^{(2)}$ - $\mu'^{(2)}_s$=0.75 mm^{-1}, while keeping the top layer optical

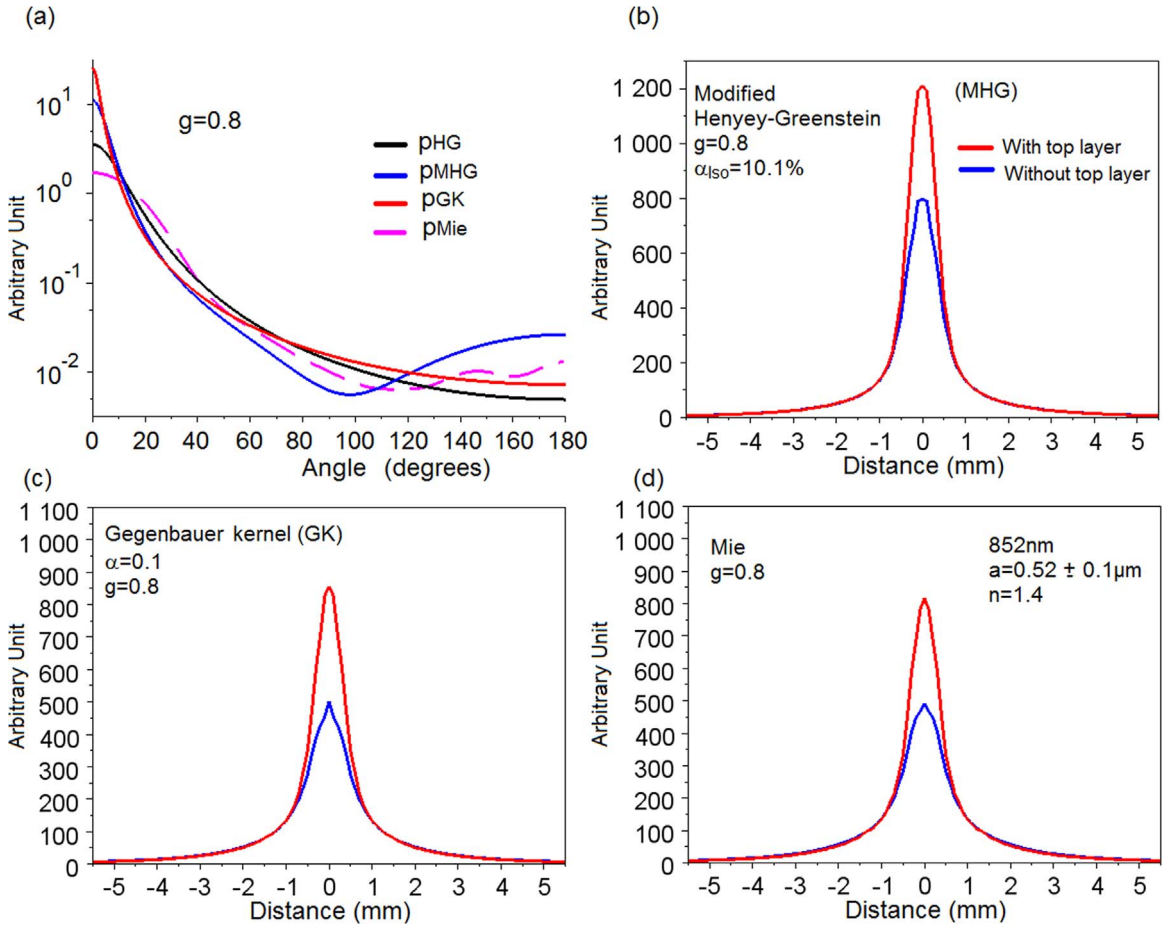

Fig. 4. Plots of (a) Scattering phase functions (Henyey-Greenstein -HG, Modified Henyey-Greenstein -MHG, Gegenbauer kernel -GK and Mie diffusion -Mie) and corresponding reflectance profiles (b-c). All the results were generated with g=0.8 and the same optical properties that those used in Fig. 3.

parameters to $\mu'_s{}^{(1)}$=4 mm^{-1} and $\mu_a{}^{(1)}$=0.05 mm^{-1}. The resulting ratios were approximately reduced by 20%, 10%, 5%, and 0.5%, respectively but were increased of 40% in case of $\mu_a{}^{(2)}$=0.0075 mm^{-1} and $\mu'_s{}^{(2)}$=0.75 mm^{-1}. As it is shown, a weak scattering and a relative absorption of the bottom layer contribute to enhance the influence of the high scattering top layer.

Fig. 3(c) shows the effect due to the change of a Gaussian light source shape into a flat distribution on the reflectance profiles. It can be observed that the previous ratio decreases from ~1.8 to ~1.5, comparable to the ones computed for a high scattering and weak absorption bottom layer. Fig. 3(d) displays the influence of the angular variation of the light source at the surface of the two-layer tissue. Notice that this light source type does not modify the reflectance in case of single bottom layer, but increases the peak intensity when the two-layer tissue is considered. Photons which strike the tissue with an important angle, have an increased likelihood to stay longer in the high scattering top layer. As a result, an increased photons density in the top layer leads to an increased peak reflectance that is only observed for a tissue covered by a thin high scattering layer.

In contrast to the axial light source distributions (step 1), the light source distributions at the tissue surface (step 0) has an impact on the relative peak magnitudes. The axial probability densities will act on the peak reflectance (with and without top layer), whereas the radial probability densities modify the magnitudes ratio. Except for the angular variations of the light source which acts at the surface of a simple tissue layer (without top layer), the absolute reflectance values are dependent on the source light types.

4.1.2. Effect of the scattering phase functions on reflectance

For a given anisotropy factor $g=g_1=<\cos\theta>$ (first moment), different scattering phase functions $p(\theta)$ can be described through the factor $\gamma=(1-g_2)/(1-g)$, where g_2 is the second order moment computed thanks to the second Legendre polynomial $g_2=<1/2(3\cos\theta^2-1)>$. The factor γ helps to more accurately describe the scattering properties of a tissue especially for small source-detector distances [40]. For instance, the Henyey-Greenstein (Eq. 8) and the delta-Eddington (Eq. 1) phase functions use $g_2=g^2$ ($\gamma=1+g$) and $g_2=g$ ($\gamma=1$), respectively. Below, the role of γ in reflectance models is examined when g is fixed in the case of a ballistic light source distribution.

For the purpose of exploration, four scattering phase functions corresponding to p_{HG}, p_{MHG}, p_{GK} and p_{Mie} were built for g=0.8 with γ=1.8, 1.24, 1.57, and 1.75, respectively. As expected, the plots in Fig. 4(a) show differences in high-angle scattering (beyond θ=90°) between $p_{MHG}(\theta)$ and $p_{Mie}(\theta)$ with respect to $p_{HG}(\theta)$ and $p_{GK}(\theta)$. The averaged reflectance profiles computed with the phase functions p_{MHG}, p_{GK} and p_{Mie} are displayed in Fig. 4(b-d). First, only the value of γ=1.24 related to p_{MHG} leads to a noticeable change of the peak magnitude (Fig. 4(b)). The increase of the absolute values is also similar to the ones computed with the incident probability $p_{IsoForw}$ (Eq. 3). The use of the scattering phase function p_{MHG} or the isotropic light source distribution has the effect to increase the backscattering for angles θ greater than 90 degrees.

The influence of the scattering phase function on backscattered light in semi-infinite turbid media has been also quantified through the simple γ parameter [42]. More recently, another parameter $\sigma=\gamma+\Sigma_{i=3\rightarrow\infty}(-0.5)^{i-2}(1-g_i)/(1-g)$ was also defined [43] to improve the quantification. Table 3 depicts comparison between our results and those reported in Refs. [42] and [43]. It is shown that the magnitude of the computed reflectance increases as γ (or σ) decreases for a fixed μ'_s. Moreover, the reflectance decreases as μ'_s is increased for a fixed γ (or σ). These trends are in good agreement with those reported in [42,43].

Many turbid tissues such as human skin are adapted to the use of the ballistic probability $p_b(z)$ [59], but other biological media, such as blood or vegetal tissues, exhibit different mechanisms of scattering. For instance, scattering from hemoglobin cells in blood implies sieve and detour effects [60]. In the same manner, the pores space inside bio-vegetal tissues give other behaviour of light propagation [61]. That gives the opportunity to consider different source distributions, as the one defined by the Eq. (3) ($p_{Iso}(z)$). In the next sections, the cases of apple and human skin tissues are considered.

4.2. Experiments and simulation results on apple tissues

4.2.1. Transmittance-Reflectance mode

The choice of the best input light source ($p_b(z)$ or $p_{IsoForw}(z)$) was operated by considering the fruit with and without skin. A measurement based on the transmittance mode was then used in order to take into account the photon propagations through the whole part of the thin skin layer. Next, a comparison between experiments and simulation results were made.

The light sources included a He-Ne Laser emitting at 633 nm, and three C.W Laser diodes emitting at 763, 784 and 852 nm. The light produced by each laser source was transported through an optical fiber (Edmund Optics) coupled with a focusing lens (f =80 mm) in such a way that the spot diameter reaches less than 1 mm, with approximately a flat shape. The light scattered by the apple sample in transmittance and reflectance modes (Fig. 5(b) and (c)) was captured with a CCD (Charge-Coupled-Device) camera. The setup [62] is presented in Fig. 5(a). Three apple cultivars, " Royal Gala, Golden Delicious and Granny Smith " were used in transmittance and reflectance modes shown in Fig. 5(b) and (c).

Fig. 6(a) depicts the light profiles captured on the cut surface in transmittance mode, when a Golden Delicious apple (with and without skin) is illuminated by a He-Ne laser source located at z_c=3 mm. It appears that the peak of the light profile coming from the unpeeled apple is larger than the one linked to the peeled apple. This trend is observed for all varieties. Fig. 6(b) depicts the ratio of the peak magnitudes measured on the three apple cultivars with and without

Table 3
Influence on the reflectance close to the source according to characteristic parameters (γ , σ) related to different phase functions p_i. Comparison between results in this work with others ones coming from the literature.

Optical properties μ_a - μ'_s detector location ρ	**Relative reflectance $R(\rho)/R_{ef}$**		
	γ ~1.25 (p_i) or σ=0.67	**γ ~1.5 (p_i) or σ=0.95**	**R_{ef}: γ ~1.75 (p_i) or σ=1**
(i) Ref. [42] ρ=0.25 mm μ_a=0 μ'_s=1 mm^{-1}	~1.3 for γ =1.20 (p_{Mie})	~1.1 for γ =1.45 (p_{Mie})	1 for γ =1.75 (p_{Mie})
μ_a=0 μ'_s=1 mm^{-1}	~1.5 for γ =1.30 (p_{MHG})	~1.2 for γ =1.50 (p_{MHG})	1 for γ =1.70 (p_{MHG})
μ_a=0 μ'_s=1.5 mm^{-1}	~1.25 for γ =1.30 (p_{MHG})	~1.1 for γ =1.50 (p_{MHG})	
(ii) Ref. [43] ρ=0			
μ_a=0.01 mm^{-1} μ'_s=1 mm^{-1}	~2 for σ =0.67	~1.1 for σ =0.95	1 for σ =1
(iii) This work ρ=0			
Without skin			
μ_a=0.0095 mm^{-1} μ'_s=1.12 mm^{-1}	~1.8 for σ =0.67 and	~1.1 for σ =0.95 and	1 for σ=1 and γ =1.8 (p_{HG})
With skin	γ =1.24 (p_{MHG})	γ =1.57 (p_{GK})	~1 for σ~1 and γ~1.75(p_{Mie})
$\mu_a{}^{(1)}$=0.05 mm^{-1} $\mu'_s{}^{(1)}$=4 mm^{-1}	~1.6	~1.05	

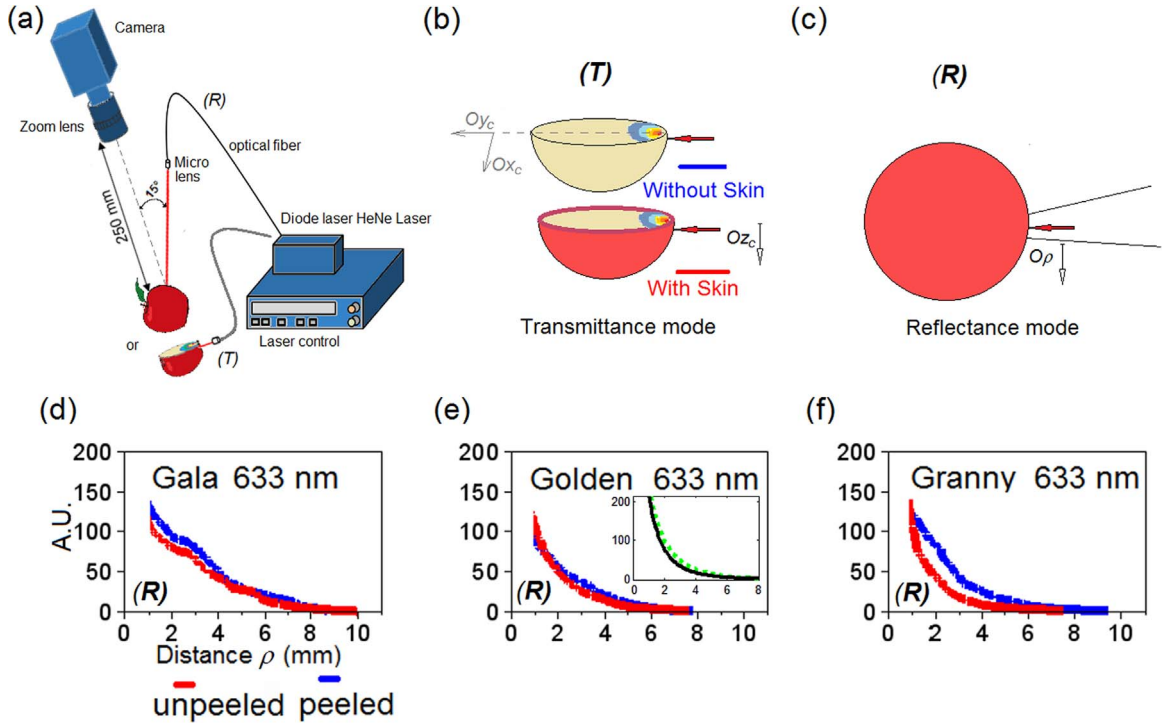

Fig. 5. (a) Experimental setup. (b) Reflectance or (c) Transmittance tissue arrangement. (*d*-f): Experimental averaged profiles obtained by the Reflectance mode (at 633 nm) for 3 apple cultivars, peeled (blue full point) and unpeeled (red full point): Royal Gala (d), Golden Delicious (e), Granny Smith (f). The insert (e) shows a simulation for a sphere with (black line) or without skin (green dotted line) obtained for the following parameters (r_s=35 mm, skin thickness=0.08 mm, $\mu'_s{}^{(2)}$=1 mm^{-1}, $\mu_a{}^{(2)}$=0.02 mm^{-1}, $\mu'_s{}^{(1)}$=4 mm^{-1}, $\mu_a{}^{(1)}$=0.6 mm^{-1}, g=0.7 and the phase function $p_{HG}(\theta)$). (For interpretation of the references to color in this figure legend, the reader is referred to the web version of this article).

skin. The case of Royal Gala provides a lower ratio than the other species. This may be explained by the fact that the Granny and Golden cultivars have a more important chlorophyll density inside their epidermis and a greater skin thickness (~90 and 80 μm, respectively) than the ones of the Gala apple (~60 μm). For all species the ratios increase with respect to the wavelength above 633 nm, and the gaps (defined in Fig. 6(b)) between the data of Golden or Granny are greater than 20%.

The observed trend may be simulated using the Monte Carlo model. A series of simulation was carried out for a fixed input light source (Eq. 3) in transmittance mode (Fig. 5(b)), when the skin layer has different optical properties and different thicknesses (described in Fig. 6(c)). The goal was to explain the gap of 0–100% displayed in the Fig. 6(b). At the source location z_c=3 mm and for a fixed skin thickness of 80 μm, the gap between the simulated profiles (with and without skin) tends to decreases when the absorption coefficient is varied from 0.05 to 0.5 mm^{-1}. But it remains unchanged when the reduced scattering coefficient was varied from 4 to 5 mm^{-1}. Moreover, increasing the skin thickness from 65 to 130 μm with similar optical parameters yields a slight decrease of the gap. However, in all the cases considered, the gap does not exceed 8%. Inspection of the results obtained by varying the scattering coefficient of about 75% or the absorption coefficient of about 40% of the flesh, while keeping the skin optical parameters fixed, reveals changes of gap of about 7% and 5%, respectively. All these results show that the large gap values found between the experiments (see Fig. 6(b)) are hardly obtained theoretically (see Fig. 6(c)).

A similar observation was found with the use of a ballistic light source (Eq. (2)). So, a model that uses the same input light source is less accurate. Another way to compare the experimental data with the simulation results may be based on the use of different input light sources according to the states peeled and unpeeled apple. The Fig. 6(d) shows the simulated case where the gap was increased to 12%: Eq. (2) and Eq. (3), respectively, for the unpeeled and peeled media. All this suggests that the mechanism of propagation of light may be considered differently with respect to the structures. For the peeled apple, there are the pores (large spaces between cells), and for the unpeeled apple, there are small cells close together and the wax layer (~2 or 3 μm). Unlike to the peeled apple, the surface of the unpeeled apple is enough smooth to use the ballistic light source distribution.

4.2.2. *Reflectance mode*

Part of reflectance curves obtained from the three apple varieties (peeled and unpeeled apples) at the wavelength of 633 nm are shown in Fig. 5(d-f). Each curve is obtained from unsaturated part of several images, after removal of the specular reflection. In the case of unpeeled apples, the Granny and Golden species give reflectance profiles with a higher slope than the cases of peeled apples. This effect is more noticeable for the Granny Smith apple. We note that the previous simulations qualitatively agree with the experimental behaviour displayed in the Fig. 5(d-f), i.e. a greater slope of the reflectance at proximity of the source when the skin is present. To precise the comparison, simulations were run with typical values that are listed Table 1 ($\mu_s{}'^{(2)}$=1 mm^{-1}, $\mu_a{}^{(2)}$=0.02 mm^{-1}, $\mu_s{}'^{(1)}$=4 mm^{-1}, $\mu_a{}^{(1)}$=0.6 mm^{-1}, g=0.7 and $p_{HG}(\theta)$) for a Golden Delicious apple (skin thickness 0.08 mm) illuminated at 633 nm. The trend about the greater slope of the profile due to the skin (insert in Fig. 5(e)) is similar to experiment. Nevertheless, the experimental mean profiles seem more spread out than the simulation ones of the case unpeeled, meaning that properties of the photon transport differs strongly between peeled and unpeeled apples.

The reflectance profiles related to Golden species have been obtained at the wavelengths of 784 and 852 nm. The optical parameters of the Golden peeled were retrieved (~10% of relative error) by using an optimal source-detector distance range [3–10 mm] for the curves fit: μ_a=0.0085 mm^{-1}- μ'_s=1.13 mm^{-1} and μ_a=0.0138 mm^{-1}- μ'_s=1.06 mm^{-1} at the wavelengths of 784 and 852 nm, respectively. We note that the profiles derived from the model are not quite similar to those obtained experimentally at distance close to the source. This may be explained by the defects of the imaging system after signal processing. Then only the relative magnitude of the peaks can be used

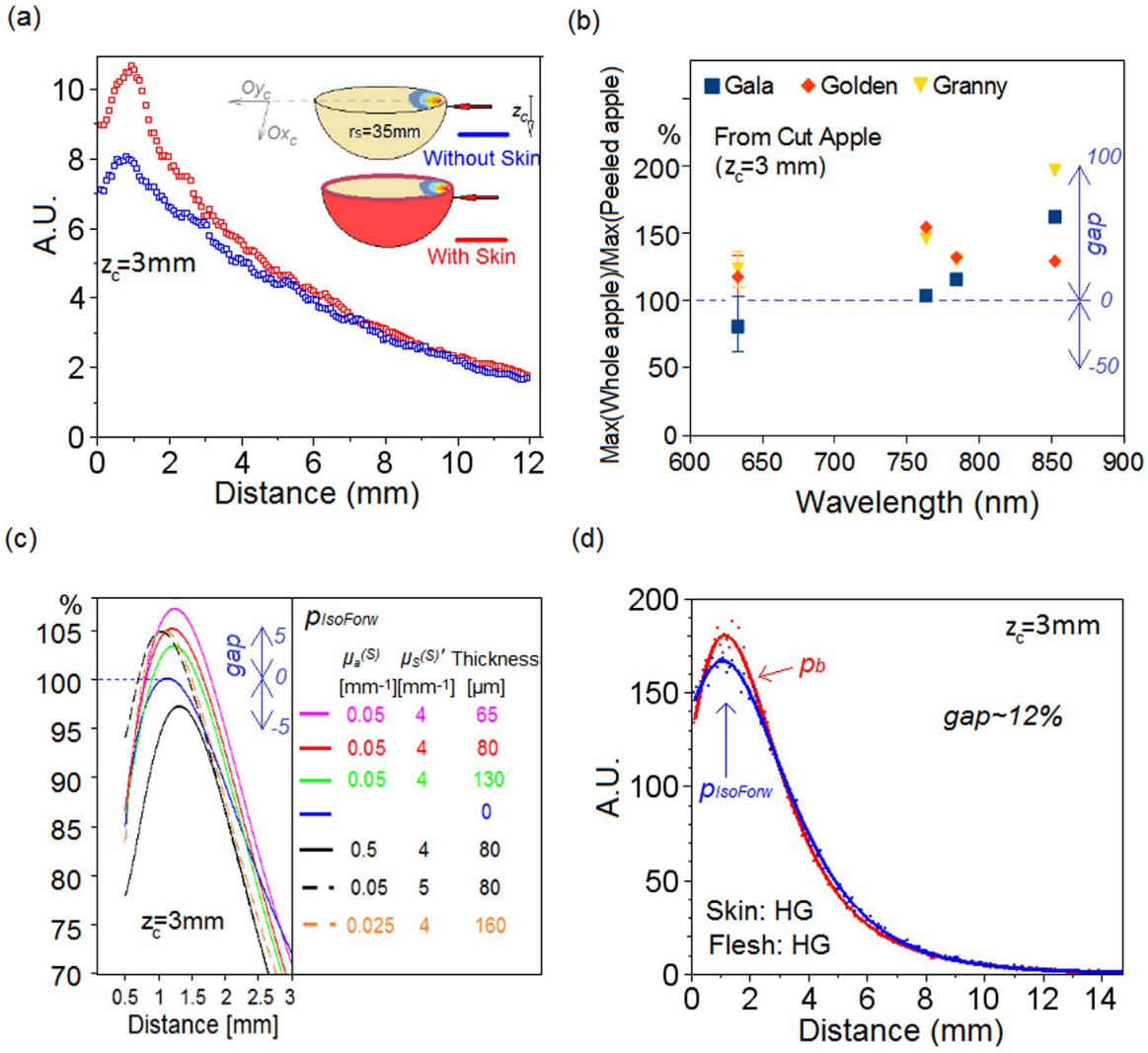

Fig. 6. Experimental averaged profiles, with skin (red) and without skin (blue), obtained in Transmittance mode at the surface of half-cut apples and z_c=3 mm. (a) Golden apple for 633 nm. (b) Ratio of peak intensities versus the wavelength. (c) Reflectance profiles extracted from simulation results with a neural network fitting (different skin layers, input $p_{IsoForw}(z)$). (d) Simulated scattered light profiles where $p_b(z)$ (Eq. (2)) and $p_{IsoForw}(z)$ (Eq. (3)) are used for the unpeeled and peeled media, respectively. Flesh optical coefficients are identical to those used in Fig. 3. (For interpretation of the references to color in this figure legend, the reader is referred to the web version of this article).

between experimental images that have been identically processed. Afterwards, the comparison between the computed peak magnitudes for unpeeled apple and peeled apple can be made according to the estimates of phase function or the type of input light source.

4.2.3. *Experimental and simulated scattering phase functions*

A goniometer setup previously tested [63,64] was used to measure the scattering angular deviations up to 160° from the skin (thickness~150 μm) and flesh samples (~290 μm and taken at 3 mm beneath the surface) extracted from a Golden apple at wavelengths 784 nm (see Fig. 7(a-b)) and 852 nm. A modified Henyey-Greenstein phase function $p_{MHG}(\theta)$ (Eq. 8) was used to fit these experimental data and provides the characteristics of an effective scattering phase function corresponding to a specific tissue [64]. For the skin sample (see Fig. 7(b)), the

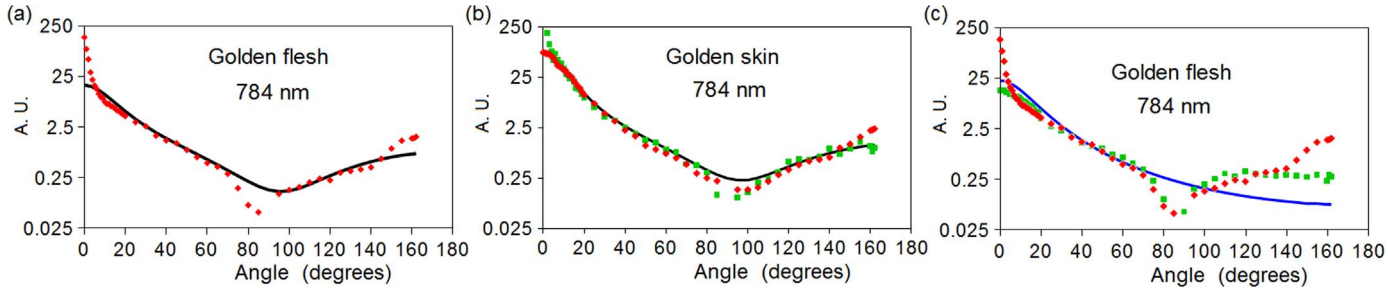

Fig. 7. Experimental effective phase functions (red diamond) obtained with a goniometer set-up. (a) and (c) flesh sample (~290 μm), (b) skin sample (~150 μm). Data fitted with analytical functions $p_{MHG}(\theta)$ (black line) or $p_{HG}(\theta)$ (blue line). Data fitted with Monte Carlo simulations of slab (green squares): case skin sample (b) with two-layer parameters (skin-flesh) (thickness$^{(1)}$=80 μm-$\mu_s^{(1)}$=15.5 mm^{-1}-$\mu_a^{(1)}$=0.1 mm^{-1}), (thickness$^{(2)}$=60 μm-$\mu_s^{(2)}$=4 mm^{-1}-$\mu_a^{(2)}$=0.01 mm^{-1}), $p_{MHG}(\theta)$ (g_{HG}=0.867-α_{Iso}=0.147); case flesh sample (c) with parameters (flesh) (thickness=0.3 mm-$\mu_s^{(2)}$=4 mm^{-1}-$\mu_a^{(2)}$=0.01 mm^{-1}), $p_{HG}(\theta)$.(g=0.74). (For interpretation of the references to color in this figure legend, the reader is referred to the web version of this article).

parameters [64] (g_{HG}~0.81, α_{Iso}~0.20) were found for both cases 784 and 852 nm, yielding an anisotropy $g=(1-\alpha_{Iso})g_{HG}$~0.65. For the flesh sample (see Fig. 7(a)), the parameters [64] (g_{HG}~0.74 and 0.8, α_{Iso}~0.29 and 0.37 for 784 and 852 nm, respectively) lead to a low value of anisotropy ~0.5.

For this last case, the modified Henyey-Greenstein function is more sensitive to the data recorded at angles ranging from 20° to 140° (see Fig. 7(a)), and does not take into account the high peak seen before 6°. Furthermore, because the thickness of the flesh sample is close to $1/\mu_t$ (mean free path) and the sample is not smooth, the detection of light far from the zero angle may be related to more than a single scattering event. Then, the value of the effective anisotropy due to k scattering events is equal to g_1^k [65], when g_1 is defined as the anisotropy of one single scattering event. When only the Henyey-Greenstein function is considered (Fig. 7(c)) on the range ($10°\leq\theta\leq90°$), the single scattering event should dominate [64], which gives a better estimate of the anisotropy coefficient $g=g_{HG}$=0.74 or 0.8 (i.e. ~$0.5^{1/2.3}$ or ~$0.5^{1/3}$).

To confirm this result, Monte Carlo simulations were run by considering a thin slab with the following parameters (thickness: 300 μm, $\mu_s^{(2)}$=4 mm^{-1}, $\mu_a^{(2)}$=0.01 mm^{-1} and g=0.74) and using a Henyey-Greenstein function p_{HG}. The scattering coefficient was chosen in such a way that the optical thickness be equal to 1.2. The simulated results (square symbols in Fig. 7(c)) are compared to the experimental phase function found in the case of the flesh. Between 10° and 140° the simulated data are close to those obtained by the experiments.

For the case of the skin sample, another anisotropy coefficient was also estimated thanks to simulations by Monte Carlo performed with a multilayer thin slab using a modified phase function $p_{MHG}(\theta)$ and two bulk tissues (thickness$^{(1)}$=80 μm, $\mu_s^{(1)}$=15.5 mm^{-1}, $\mu_a^{(1)}$=0.1 mm^{-1} and thickness$^{(2)}$=60 μm, $\mu_s^{(2)}$=4 mm^{-1}, $\mu_a^{(2)}$=0.01 mm^{-1}). After several tries, the fit of the experimental phase function (see square symbol of Fig. 7(b)) with values of g_{HG}=0.867, αIso~0.147 was considered as sufficient (anisotropy ~0.74). So according to this numerical retrieval method, flesh and skin have two different phase functions but the same anisotropy coefficient. The simulated results obtained with the two-layer model can now be used with the previous data [64] or these new retrieval information.

4.2.4. Experimental reflectance profiles versus simulations

First, the experimental data of the Fig. 8 were built with different parts, coming from saturated and unsaturated images corresponding to the wavelength of 852 nm. For the two-layered configuration, three cases were simulated using a ballistic source: Gaussian and uniform radial source with the effective phase function $p_{MHG}(\theta)$, Gaussian radial source with only $p_{HG}(\theta)$. The optical parameters of the skin (g=0.64–0.65 [64], $\mu_a^{(1)}$=0.1 mm^{-1}, $\mu'^{(1)}_s$=4 mm^{-1}, thickness=80 μm) were chosen in this first approach. As seen in Fig. 8(a), the simulations using the effective modified phase function have given profiles too narrow compared to the experimental data. The uniform source, who is more appropriated for the flat beam at the exit of the fiber, enlarges slightly the profiles. When only the part $p_{HG}(\theta)$ is taken into account for the flesh, the model seems well adapted to simulate the experiment features. Subsequently, the Henyey-Greenstein function will be only considered for the flesh layer ($g=g_{HG}$=0.8 or 0.74 for 852 and 784 nm, respectively).

Second, the profiles extracted from 21 images, related to a wavelength of 784 nm, are used to build an average profile [62]. The uniform radial distribution for the incident photons was used and the density $p_{MHG}(\theta)$ for the skin layer were defined with the previous [64] or new retrieved parameters. The maximum value related to the two-layer system is larger than the one related to the peeled system, as shown in Fig. 9(a), whatever are the estimated modified phase functions (effective [64] or single phase function of the skin layer). But the discrepancy between the peak profiles differs rather with respect to the light source types used for the peeled apple: wrong for the case $p_b(z)$ (Eq. 2) contrary to the case $p_{IsoForw}(z)$ (Eq. 3). Other comparisons, such as the one depicted in Fig. 8(b) where the peaks are not averaged and where the effective phase function of the skin is used, give similar trends.

In order to see the influence of the phase function type on the simulations comparison, other functions were considered with the same anisotropy 0.74. The factors γ (defined in the Section 4.1.2) were computed for all the cases studied. In Fig. 9(b), the functions p_{GK} and p_{MGK} are chosen (with α=0.1) for the flesh and the skin, respectively. A similar behaviour as the one obtained for p_{HG} and p_{MHG} (Fig. 9(a)) is observed. Both cases show a difference between the factors γ of the flesh and the skin almost equal to 0.6. In Fig. 9(c), phase functions computed from the Mie diffusion are used with γ particularly great but close (skin: 1.94 and flesh: 1.97). This time, the gap between the peak intensities differs of the experimental gap whatever the light input sources. A phase function linked to the skin layer including a Rayleigh component has the effect to give a smaller factor γ than the phase function linked to the flesh layer. As a result, a comparison can be made properly between an unpeeled apple model that uses a ballistic source and the peeled apple that uses a diffusive input source. Note that the average radius of the spherical particles, which allows to find the same values of anisotropy coefficient by the Mie diffusion, are 0.34 μm for

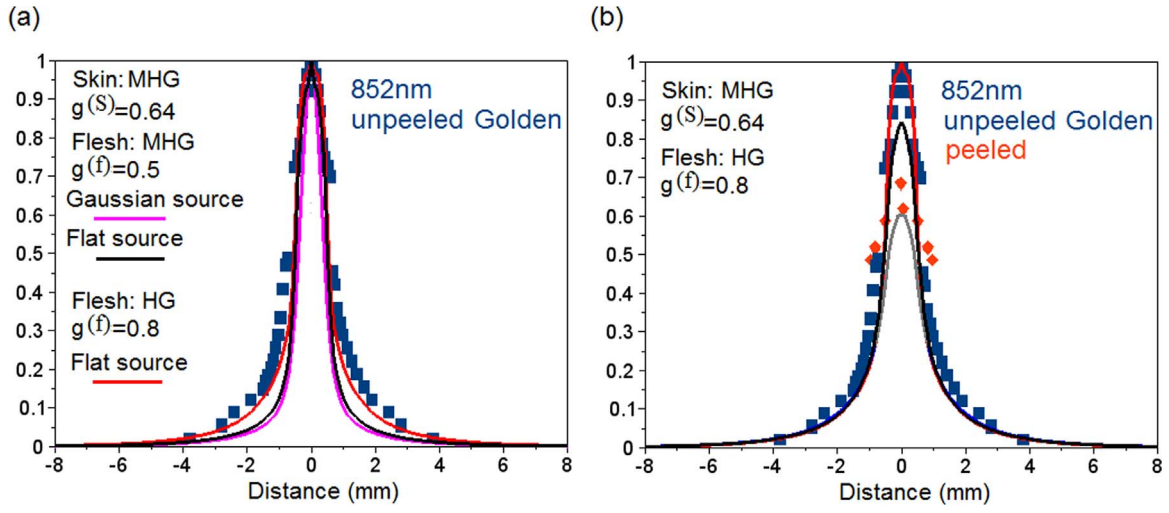

Fig. 8. Experimental (symbols) and numerical (lines) peaks of light reflected by a Golden apple. (a) $p_{MHG}^{(1)}$, $g^{(1)}$=0.64, $p_{MHG}^{(2)}$, $g^{(2)}$=0.5 or $p_{HG}^{(2)}$, $g^{(2)}$=0.8. (b) Flat source and $p_{MHG}^{(1)}$, $g^{(1)}$=0.64, $p_{HG}^{(2)}$, $g^{(2)}$=0.8. Grey and black lines correspond to the Eq. (2) and Eq. (3), respectively. (For interpretation of the references to color in this figure legend, the reader is referred to the web version of this article).

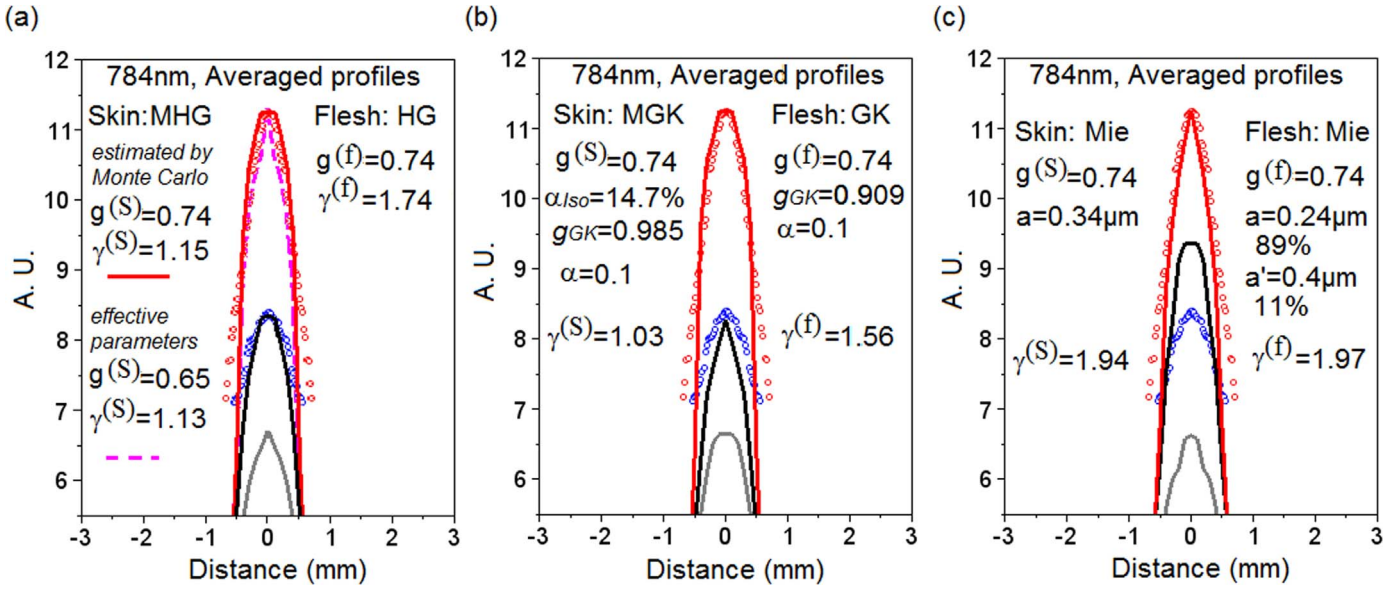

Fig. 9. Experimental (symbols) and numerical (lines) peaks of light reflected by a Golden apple (a-c) and half-cut apple (d), at the wavelength of 784 nm. Grey and black lines correspond to the Eq. (2) and Eq. (3), respectively. Several phase functions p and anisotropies g are used for the flesh (2) and the skin (1). (a) $p_{MHG}^{(1)}$ [α_{Iso}=0.147], $g^{(1)}$=0.74 or $p_{MHG}^{(1)}$ [α_{Iso}=0.196], $g^{(1)}$=0.65 [dashed line], $p_{HG}^{(2)}$, $g^{(2)}$=0.74; (b) $p_{MGK}^{(1)}$, $g^{(1)}$=0.74, $p_{GK}^{(2)}$, $g^{(2)}$=0.74; (c) $p_{Mie}^{(1)}$, $g^{(1)}$=0.74, $p_{Mie}^{(2)}$, $g^{(2)}$=0.74.

the skin, and a combination of 0.24 μm (89%) and 0.4 μm (11%) for the flesh, when the index ratio m=1.4/1 and the wavelength 784 nm is chosen. These sizes are in agreement with the average size of biological cell components [30].

Owing to the use of distinct light source input according the state peeled or not peeled, the comparison between simulation and experiment was carried out. In order to optimize the Monte Carlo model, the phase function of the skin layer exhibited an increase of its back-scattered part contrary to the phase function of the flesh. If the simulation does not take into account this specify, an error can be perceived on the peak of the reflectance profile. In our model, the magnitude order of this error is estimated as equal to the error obtained when the skin thickness is changed of 10 μm (~10% of the mean thickness).

4.3. Human skin tissues

For a two-layer model where the ballistic source is sufficient, the influence of the skin layer on the peak reflectance can be settled by an appropriate choice of phase function, for which the asymmetry factors g and γ are close to the experimental values. The modified phase function is an easy way to do it. This was shown here for simulation of an apple irradiated with a laser source directed normally to its surface. But the simulations on human skin illumination requires another model with an appropriate phase function. In the next subsections, the problem of the phase function and the influence of source distribution are approached for a human skin model.

4.3.1. Bidirectional Reflectance Distribution Function (BRDF)

Light may exhibit scattering and/or directional properties at the skin surface according to the incident angles. The reflectance coming

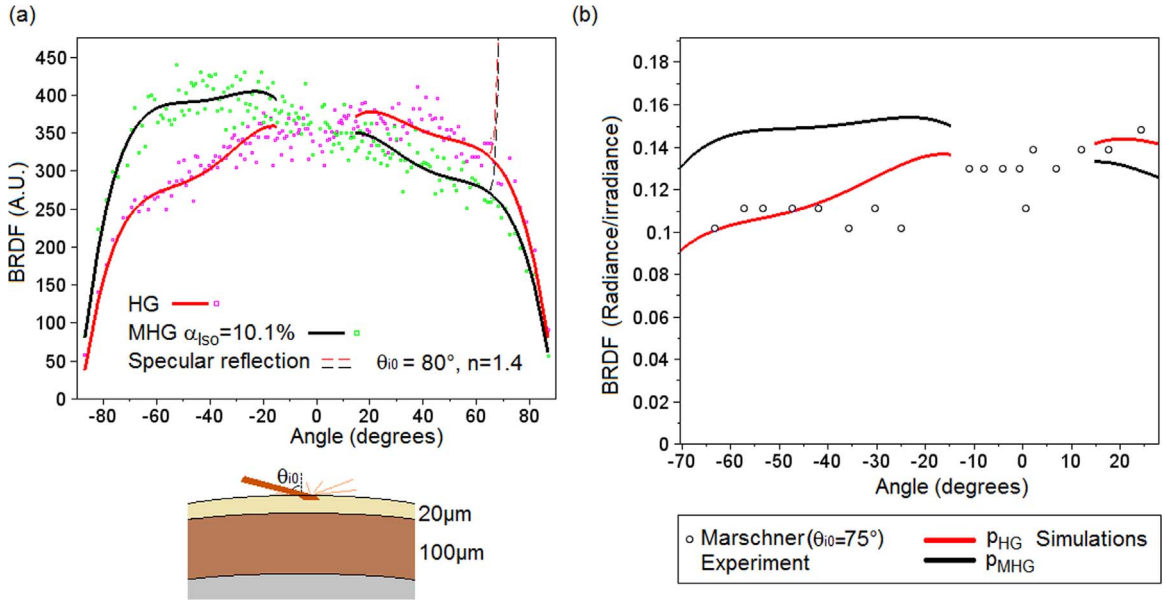

Fig. 10. (a) BRDF (Bi-directional Reflectance distribution functions) computed with an incident angle of 80°, a Henyey-Greenstein or a modified Henyey-Greenstein phase function and r_s=70 mm. (b) The fittings of the data in (a) are compared with experimental data (empty symbols) estimated from Marschner et al. [66].

from the incident source location is characterized by the Bidirectional Reflectance Distribution Function (BRDF) [49,61]. As expected this function is sensitive to the incident photons and to the direction deflection probabilities. Then, the angular distribution of the source and the phase function may impact the shape and the amplitude of this BRDF. In order to observe this, a simplified scheme of the human skin is proposed, with different optical parameter sets μ_a=0.8, 0.4, and 0.3 mm^{-1}, μ_s=100, 45, and 19 mm^{-1}, g=0.86, 0.8, and 0.8 for the stratum corneum, epidermis and dermis layers, respectively.

First, with an incident angle of −80°, i.e. a transmitted angle of 44.7°, the BRDF are obtained with a Henyey-Greenstein function and a modified Henyey-Greenstein phase function with α_{Iso}=10.1% (Fig. 10(a)). Outside the area of the specular reflection, the scattering occurs and it can be seen for angles < 60° that the phase function changes the shape of the reflectance according to the emitting angle. A comparison was made with experimental data reported by Marschner et al. [66], who used an electronic flash illumination on several human forehead at an incident angle of 75° (Fig. 10(b)). The comparison was focused on the angular domain where the Fresnel reflection is not predominant. That allows to prove that the Henyey-Greenstein phase function, often used in simulation codes of human skin [16,17,67,68], is well adapted to the optical study of the stratum corneum and epidermis layers.

4.3.2. Light penetration in the human skin

Second, the amplitude variation of the BRDF with respect to the source is considered. The needed quantity of absorbed light in the dermis according to the phototherapy technics depends on an accurate dose of light injected at the surface. The Eq. (5) and Eq. (2), together with a Henyey-Greenstein phase function, are used with the parameter n=infinite (normal injection θ_0=0) or n=1 (angular density distribution $1/\pi.\cos\theta_0$). That expression simulates a collimated (n=infinite) or a Lambertian distribution of the source (n=1) inside the medium. As shown in Fig. 11(a), the BRDF increases with the Lambertian distribution, while the light penetration in the tissue decreases. Simulation results about the light penetration have been also considered but with respect to two different stratum corneum layers: large thickness (20 μm) and scattering coefficient (100 mm^{-1}), or small thickness (10 μm) and scattering coefficient (50 mm^{-1}). The Fig. 11(b) shows the light transmission along the optical axis through the stratum corneum, the epidermis and the upper dermis. Relatively to the normal injection, the Lambertian source distribution produces a higher photon density for the stratum corneum layer and a smaller photon density for the upper dermis layer. We note that there is the same photon density level inside the dermis for the two considered stratum corneum layers. The light density occurring in the dermis depends more on the angular distribution of the light input source than the amount of dead cells covering the epidermis surface.

5. Conclusion and summary

The propagation of light in curved turbid media covered with a thin tissue layer has been studied thanks to a multi-layered Monte Carlo model. The reflectance profiles obtained with a two-layer system were systematically compared to the ones related to the homogeneous system without top layer. Owing to the fact that this first layer is considered as having strong diffusing and absorbing properties, the photons will concentrate largely in the vicinity of the light source. The light close to the source depends on both the light source distribution, on the surface (radially or angularly) and inside the volume (axially), and on the scattering phase function. Thus, the scattering phase functions were varied, and the -radial, -angular and -axial distributions of the input light source were introduced as another constraints. All these distributions have been inserted as variable functions in the first steps of the Monte Carlo code.

The peak intensity of the reflectance profiles have been seen as very sensitive to the variation of each light source distribution, and to the characteristic parameter γ linked to each considered scattering phase function. The ratio of the peak intensities, with or without skin, remains unchanged except for changing the radial distributions (Gaussian source versus uniform source) and the angular distributions, and is slightly affected by the modified Henyey-Greenstein phase function.

A curved two-layer turbid model is well adapted to study the light

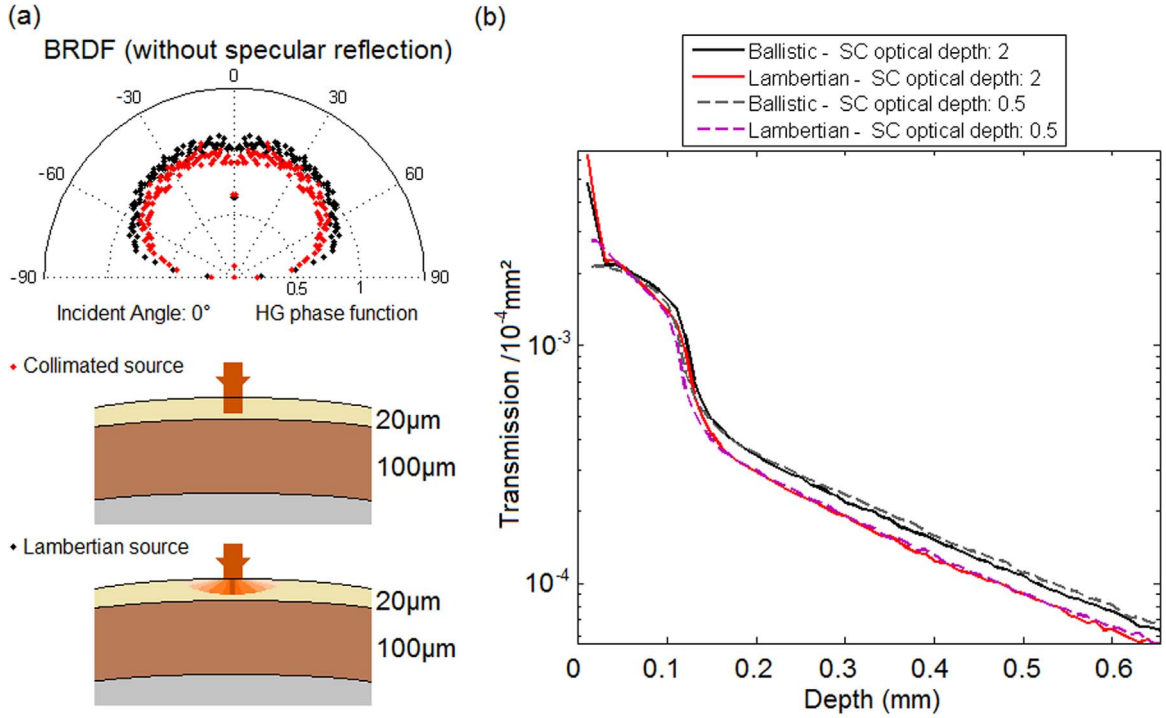

Fig. 11. (a) BRDF computed with an incident angle of 0°, a Henyey-Greenstein phase function, and with a ballistic or Lambertian source. (b) Depth light penetration in the turbid medium with two input light sources (as in (a)), but with two optical lengths of Stratum Corneum layer: 2 (thickness 20 μm *μ_s=100 mm^{-1}) or 0.5 (thickness 10 μm *μ_s=50 mm^{-1}).

propagation in fruits such as apples. Experiments were performed on three apple species by using multispectral imaging and several laser sources emitting in the visible and near-infrared domain. Light reflectance of the three apples have shown different behaviour from each other, which seems related to the thickness and the pigments density of their peel. The peak intensity of reflectance on the planar surface of a half-sphere were also considered when the source is located on the curved surface but close to the cut surface (a partial transmittance mode). This transmittance mode allows to characterize the axial distribution of the light source. Moreover, some experimental phase functions were provided by a goniometer setup for skin and flesh samples extracted from one cultivar. Monte Carlo models were adjusted by the use of experimental phase functions, in order to compare simulated reflectance profiles with those recorded by the imaging setup.

Therefore, it was shown that a modified Henyey-Greenstein function is well appropriate to simulate the light propagation through the peel layer, while the axial distribution of the incident photons computed in the case of a peeled apple is distinct from the one related to an unpeeled apple. This may be explained by the fact that the flesh structure contains cells and pores whereas the skin structure comprises small cells but without pore spaces. These computations contribute to separate the different factors that shape the diffuse reflectance profiles and could lead to improved models for fruit quality inspection.

The angular dependence of the reflection of a human skin has been also simulated to illustrate the effects of distribution functions on a biological tissue. It was shown that a Henyey-Greenstein function was appropriate to simulate the light propagation in the visible wavelength range. Moreover at the first attempt, the difference on the depth propagation of light inside a human skin has been studied between a light source having Lambertian angular distribution and a light under normal incidence. The penetration of light, depending on the reflectance magnitude, is perceived as being more affected by the input light source distribution than for the state of the stratum corneum (i.e. related to quantity and size of the dead cells).

The investigation on the scattering events inside the skin and flesh tissues should be made in a future work for different fruit specimens and for other wavelengths ranging from 400 nm to 1000 nm. Concerning the real human skin model, the roughness of the surface and the blood vessel absorption in the dermis should be taking into account in the Monte Carlo model. Furthermore, a well-conceived Monte Carlo model can help in the improvement of the retrieval of coefficients near the skin region. In particular, the knowledge on the mechanism of scattering for the first injected photons can be useful to the fast hybrid-Monte Carlo processes.

Acknowledgements

This work was funded by the Regional Council of Pays de la Loire and supported by the AI fruit Project.

References

[1] V.V. Tuchin, Tissue Optics: Light scattering methods and Instruments for Medical Diagnosis, 2nd ed., SPIE, Bellingham, 2007.
[2] R.G. Wheeland, Clinical uses of lasers in dermatology, Lasers Surg. Med. 16 (1995) 2–23.
[3] G. Teikemeier, D.J. Goldberg, Skin resurfacing with the erbium-YAG laser, Dermatol. Surg. 23 (1997) 685–687.
[4] M. Cope, D.T. Delpy, System for long-term measurement of cerebral blood and tissue oxygenation on newborn infants by near infra-red transillumination, Med. Biol. Eng. Comput. 26 (1988) 289–294.
[5] C. Donner, H.W. Jensen, Light diffusion in multilayered translucent materials, ACM Trans. Graph. 24 (3) (2005) 1032–1039.
[6] B. Nicolaï, K. Beullens, E. Bobelyn, A. Peirs, W. Saeys, K. Theran, J. Lammertyn, Non destructive measurement of fruit and vegetable quality by means of NIR spectroscopy: a review, PostHarvest Biol. Technol. 46 (2) (2007) 99–118.
[7] J. Lammertyn, A. Peirs, J. De Baerdemaeker, B. Nicolaï, Light penetration properties of NIR radiation in fruit with respect to non-destructive quality assessment, Post Harvest Biol. Technol. 18 (2000) 121–132.
[8] K.M. Yoo, F. Liu, R.R. Alfano, When does the diffusion approximation fail to describe photon transport in random media?, Phys. Rev. Lett. 64 (1990) 2647–2650.
[9] A. Ishimaru, Diffusion of light in turbid material, Appl. Opt. 28 (1989) 2210–2215.
[10] A. Liemert, A. Kienle, Light transport in three-dimensional semi-infinite scattering media, J. Opt. Soc. Am. A 29 (7) (2012) 1475–1481.
[11] L.H. Wang, S.L. Jacques, L.Q. Zheng, MCML-Monte Carlo modeling of light transport in multilayered tissues. Comput, Methods Prog. Biol. 47 (2) (1995) 131–146.
[12] F. Vaudelle, J.P. L'Huillier, Influence of the size and skin thickness of apple varieties on the retrieval of internal optical properties using vis/Nir spectroscopy: a Monte Carlo-based study. Comput. electron, Comput. Electron. Agric. 116 (2015) 137–149.
[13] S. Mordechai, Applications of Monte Carlo Method in Science and Engineering, InTech, Rijeka, Croatia, 2011.
[14] G. Zaccanti, Monte Carlo study of light propagation in optically thick media: point source case, Appl. Opt. 30 (1991) 2031–2041.
[15] T. Lister, P.A. Wright, P.H. Chappell, Optical properties of human skin, J. Biomed. Opt. 17 (9) (2012) 090901.
[16] R. Eze, S. Kumar, Laser transport through thin scattering layers, Appl. Opt. 49 (2010) 358–368.
[17] I.V. Meglinski, S.J. Matcher, Quantitative assessment of skin layers absorption and skin reflectance spectra simulation in the visible and near-infrared spectral regions, Physiol. Meas. 23 (2002) 741–753.
[18] C. Mansouri, J.P. L'Huillier, N.H. Kashou, A. Humeau, Depth sensitivity analysis of functional near-infrared spectroscopy measurement using three-dimensional Monte Carlo modelling-based magnetic resonance imaging, Lasers Med Sci. 25 (2010) 431–438.
[19] F. Vaudelle, J.P. L'Huillier, Time-resolved optical fluorescence spectroscopy of heterogeneous turbid media with special emphasis on brain tissue structures including diseased regions: a sensitivity analysis, Opt. Commun. 304 (2013) 161–168.
[20] E. Berrocal, I.V. Meglinski, D.A. Greenhalgh, M.A. Linne, Image transfer through the complex scattering turbid media, Laser Phys. Lett. 3 (9) (2006) 464–467.
[21] E. Berrocal, D.L. Sedarsky, M.E. Paciaroni, I.V. Meglinski, M.A. Linne, Laser light scattering in turbid media Part I: experimental and simulated results for the spatial intensity distribution, Opt. Express 15 (17) (2007) 10649–10665.
[22] T. Okamoto, T. Kumagawa, M. Motoda, T. Igorashi, K. Nakao, Monte Carlo simulation of light reflection from cosmetic powder particles near the human skin surface, J. Biomed. Opt. 18 (2013). http://dx.doi.org/10.117/1.JBO 18.6.061232.
[23] L.L. Xue, C.P. Zhang, X.Y. Wang, M. Zhu, Yao, L.S. Zhang, R.H. Chi, J.D. Zhang, G.Y. Zhang, Monte Carlo simulation of light transport in five-layered skin tissue, Chin. Phys. Lett. 17 (2000) 909–911.
[24] B. Nasouri, T.E. Murphy, H. Berberoglu, Near infrared laser penetration and absorption in human skin, Proc. SPIE Mech. Low.-Light Ther. IX (2014) 893207.
[25] S.L. Jacques, Light Distributions from Point, Line and Plane Sources for Photochemical Reactions and Fluorescence in Turbid Biological Tissues, Photochem. Photobiol. 67 (1998) 23–32.
[26] J.Q. Lu, X.H. Hu, K. Dong, Modeling of the rough-interface effect on a converging light beam propagating in a skin tissue phantom, Appl. Opt. 39 (2000) 5890–5897.
[27] A.N. Bashkatov, E.A. Genina, V.V. Tuchin, G.B. Altshuler, Y.V. Yaroslavsky, Monte Carlo study of skin optical clearing to enhance light penetration in the tissue: implications for photodynamic therapy of acne vulgaris (Proc. SPIE)Adv. Laser Technol. 2007 (2008).
[28] F.H. Mustafa, M.S. Jaafar, A.H. Ismail, Control light delivery in PDT by taking account the optical properties of hair density on the skin surface, Mod. Appl. Sci. 5 (2011) 149–155.
[29] W. Wang, C. Li, Measurement of the light absorption and scattering properties of onion skin and flesh at 633 nm, Postharvest Biol. Technol. 86 (2013) 494–501.
[30] R. Watté, B. Aernouts, R. Van Beers, E. Herremans, Q. Tri Ho, P. Verboven, B. Nicolaï, W. Saeys, Modeling the propagation of light in realistic tissue structures with MMC-fpf: a meshed Monte Carlo method with free phase function, Opt. Express 23 (2015) 17467–17486.
[31] M.L. Askoura, F. Vaudelle, J.P. L'Huillier, Numerical study of light transport in apple models based on Monte Carlo simulations, Photonics 3 (2) (2016). http://dx.doi.org/10.3390/photonics3010002.
[32] P. Baranowski, W. Mazurek, J. Wozniak, U. Majewska, Detection of early bruises in apples using hyperspectral data and thermal imaging, J. Food Eng. 110 (2012) 345–355.
[33] Y. Peng, R. Lu, Improving apple fruit firmness predictions by effective correction of mutispectral scattering images, Postharvest Biol. Technol. 41 (2006) 266–274.
[34] J. Qin, R. Lu, Measurement of the optical properties of fruits and vegetables using spatially resolved hyperspectral diffuse reflectance imaging technique, Postharvest Biol. Technol. 49 (2008) 355–365.
[35] A. Francini, L. Sebastiani, Phenolic compounds in apple (Malus x domestica Borkh.): compounds characterization and stability during postharvest and after processing, Antioxidants 2 (2013) 181–193.
[36] W. Saeys, M.A. Velazco-Roa, S.N. Thennadil, H. Ramon, B.M. Nicolaï, Optical properties of apple skin and flesh in the wavelength range from 350 to 2200 nm, Appl. Opt. 47 (2008) 908–919.
[37] N. Nguyen Do Trong, C. Erkinbaev, M. Tsuta, J. De Baerdemaeker, B. Nicolaï, W. Saeys, Spatially resolved diffuse reflectance in the visible and near-infrared wavelength range for non-destructive quality assessment of'Braeburn' apples, Postharvest Biol. Technol. 91 (2014) 39–48.
[38] H. Cen, R. Lu, Quantification of the optical properties of two-layer turbid materials

using a hyperspectral imaging-based spatially-resolved technique, Appl. Opt. 48 (2009) 5612–5623.
[39] J.R. Mourant, J. Boyer, A.H. Hielsher, I.J. Bigio, Influence of the scattering phase function on light transport measurements in turbid media performed with small source-detector separations, Opt. Lett. 21 (1996) 546–548.
[40] F. Bevilacqua, C. Depeursinge, Monte-Carlo study of diffuse reflectance at source detector separations close to one transport mean free path, J. Opt. Soc. Am. A 16 (1999) 2935–2945.
[41] A. Kienle, F.K. Forster, R. Hibst, Influence of the phase function on determination of the optical properties of biological tissue by spatially resolved reflectance, Opt. Lett. 26 (2001) 1571–1573.
[42] K.W. Calabro, I.J. Bigio, Influence of the phase function in generalized diffuse reflectance models: a review of current formalisms and novel observations, J. Biomed. Opt. 19 (7) (2014) 75005.
[43] N. Bodenschatz, P. Krauter, A. Liemert, A. Kienle, Quantifying phase function influence in subdiffusively backscattered light, J. Biomed. Opt. 21 (3) (2016) 035002.
[44] P. Verboven, A. Nemeth, M.K. Abera, E. Bongaers, D. Daelemans, P. Estrade, E. Herremans, M. Hertog, W. Saeys, E. Vanstreels, B. Verlinden, M. Leitner, B. Nicolaï, Optical coherence tomography visualizes microstructure of apple peel, Postharvest Biol. Technol. 78 (2013) 123–132.
[45] I. Homutová, J. Blažek, Differences in fruit skin thickness between selected apple (Malus domestica Borkh.) cultivars assessed by histological and sensory methods, Hort. Sci. 33 (3) (2006) 108–113.
[46] R. Cubeddu, C. D'Andrea, A. Pifferi, P. Taroni, A. Torricelli, G. Valentini, M. Ruiz-Altisent, C. Valero, C. Ortiz, C. Dover, D. Johnson, Time-resolved reflectance spectroscopy applied to the nondestructive monitoring of the internal optical properties in apples, Appl. Spectrosc. 55 (10) (2001) 1368–1374.
[47] P.I. Rowe, R. Künnemeyer, A. McGlone, S. Talele, P. Martinsen, R. Seelye, Relationship between tissue firmness and optical properties of 'RoyalGala' apples from 400 to 1050 nm, Postharvest Biol. Technol. 94 (2014) 89–96.
[48] R. Lu, H. Cen, M. Huang, D.P. Ariana, Spectral absorption and scattering properties of normal and bruised apple tissue, ASABE 53 (1) (2010) 263–269.
[49] T. Igarashi, K. Nishino, S.K. Nayar, The appearance of human skin: a survey, Found. Trends Comput. Graph. Vis. 3 (1) (2007) 1–95.
[50] A.N. Bashkatov, E.A. Genina, V.V. Tuchin, Tissue Optical Properties. In: Handbook of Biomedical Optics, CRC Press, 2011, pp. 67–100.
[51] J.F. Potter, The Delta function approximation in radiative transfer theory, J. Atmos. Sci. 27 (1970) 943–949.
[52] J.H. Joseph, W.J. Wiscombe, J.A. Weinman, The delta-Eddington approximation for radiative flux transfer, J. Atmos. Sci. 33 (1976) 2452–2459.
[53] F. Zhang, M. Kinnunen, A. Popov, R. Myllylä, Monte Carlo method for simulating optical coherence tomography signal in homogeneous turbid media, Proc. SPIE 7022 (2008) 702213.
[54] T.F. Chen, G.V.G. Baranoski, K.F. Lin, Bulk scattering approximations for HeNe laser transmitted through paper, Opt. Express 16 (2008) 21762–21771.
[55] C.F. Bohren, D.R. Huffman, Absorption and Scattering of Light by Small Particles, Wiley, New-York, 1983.
[56] L.G. Henyey, J.L. Greenstein, Diffuse radiation in the galaxy, Astrophys. J. 93 (1941) 70–83.
[57] L.O. Reynolds, N.J. McCormick, Approximate two-parameter phase function for light scattering, J. Opt. Soc. Am. 70 (1980) 1206–1212.
[58] S.L. Jacques, C.A. Alter, S.A. Prahl, Angular dependence of HeNe laser light scattering by human dermis, Laser Life Sci. 1 (1987) 309–334.
[59] X. Deulin, J.P. L'Huillier, Finite element approach to photon propagation modelling in semi-infinite homogeneous and multilayered tissue structures, EPJ Appl. Phys. 33 (2006) 133–146.
[60] L. Northam, G.V.G. Baranoski, A novel first principles approach for the estimation of the sieve factor of blood samples, Opt. Express 18 (2010) 7456–7469.
[61] P. Hanrahan, W. Krueger, Reflection from Layered Surfaces due to Subsurface Scattering. In: Proceedings of the SIGGRAPH '93 Addison-Wesley Publishing Company, New-York. 1993, pp. 165–174.
[62] M.L. Askoura, F. Vaudelle, J.P. L'Huillier, Experimental study of light propagation in apple tissues using a multispectral imaging system, Photonics 3 (50) (2016). http://dx.doi.org/10.3390/photonics3030050.
[63] J. Choukeife, J.P. L'Huillier, Measurements of scattering effects within tissue-like media at two wavelengths of 632.8 nm and 680 nm, Lasers Med. Sci. 14 (1999) 286–296.
[64] M.L. Askoura, F. Vaudelle, J.P. L'Huillier, Multispectral measurement of scattering-angular light distribution in apple skin and flesh samples, Appl. Opt. 55 (32) (2016) 9217–9225.
[65] J. Piskozub, D. McKee, Effective scattering phase functions for the multiple scattering regime, Opt. Express 19 (2011) 4786–4794.
[66] S.R. Marschner, S.H. Westin, E.P.F. Lafortune, K.E. Torrance, D.P. Greenberg, Image-Based BRDF Measurement Including Human Skin. Rendering Techniques' 99 in: Proceedings of the 10th Eurographics Workshop on Rendering, Granada, 1999, pp. 139–152.
[67] A.E. Karsten, A. Singh, M.W. Braun, Experimental verification and validation of a computer model for light–tissue interaction, Lasers Med. Sci. 27 (2012) 79–86.
[68] Breault Research Organisation, Realistic Skin Model (RSM)-BIO Toolkit Interactive Script for ASAP, ASAP Technical Publication BROPN1177-RSM, Breault Research Organisation, Inc., 2008.